1 **An iterative algorithm to simultaneously retrieve aerosol extinction and effective radius profiles using**

2 **the CALIOP lidar**

3 Liang Chang[1], Jing Li[1,2 #], Jingjing Ren [3], Changrui Xiong[1], Lu Zhang [4,5]

4 *[1] Department of Atmospheric and Oceanic Sciences, School of Physics, Peking University, Beijing 100871,*

5 *China*

6 *[2]Collaborative Innovation Center on Forecast and Evaluation of Meteorological Disasters (CIC-FEMD),*

7 *Nanjing University of Information Science & Technology, Nanjing, 210044, China*

8 *[3] Intelligent Science & Technology Academy Limited of CASIC*

9 *[4] Key Laboratory of Radiometric Calibration and Validation for Environmental Satellites, National Satellite*

10 *Meteorological Center (National Center for Space Weather), China Meteorological Administration, Beijing*

11 *100081, China*

12 *[5] Innovation Center for FengYun Meteorological Satellite (FYSIC), Beijing 100081, China*

13 *# Correspondence to*: Jing Li (jing-li@pku.edu.cn)

14 **Abstract**

15 The Cloud-Aerosol Lidar with Orthogonal Polarization (CALIOP) onboard the Cloud-Aerosol Lidar and

16 Infrared Pathfinder Satellite Observation (CALIPSO) satellite has been widely used in climate and

17 environment studies to obtain the vertical profiles of atmospheric aerosols. To retrieve the vertical profile of

18 aerosol extinction, the CALIOP algorithm assumes column-averaged lidar ratios based on a clustering of

19 aerosol optical properties measured at surface stations. On one hand, these lidar ratio assumptions may not

20 be appropriate or representative at certain locations. One the other hand, the two-wavelength design of

21 CALIOP has the potential to constrain aerosol size information, which has not been considered in the

22 operational algorithm. In this study, we present a modified inversion algorithm to simultaneously retrieve

23 aerosol extinction and effective radius profiles using two-wavelength elastic lidars such as the CALIOP.

Specifically, a look-up table is built to relate the lidar ratio with the Ångström exponent calculated using aerosol extinction at the two wavelengths, and the lidar ratio is then determined iteratively without a priori assumption. The retrieved two-wavelength extinction at each layer is then converted to particle effective radius assuming a lognormal distribution. The algorithm is tested on synthetic data, Raman lidar measurements and then finally the real CALIOP backscatter measurements. Results show improvements over the CALIPSO operational algorithm by comparing with ground-based Raman lidar profiles.

1 Introduction

Atmospheric aerosols have important impacts on the physical and chemical processes in atmosphere, as well as the climate system and public health. Optical properties of aerosols are critical in quantifying their radiative effects in the Earth's climate system. Moreover, the vertical distribution of aerosol properties, such as its extinction coefficient and particle size, is one of the key elements to assess climate effect (IPCC, 2023). Direct aerosol radiative forcing, which plays an important role in the Earth's energy budget, is impacted by the vertical distribution of aerosols, especially that for absorbing aerosols (Goto et al., 2011; Eswaran et al., 2019; Zhang et al., 2022). The vertical profiles of aerosol optical properties is also essential estimating the solar heating rate (Kudo et al., 2016), and establishment of aerosol parameterization schemes for satellite remote sensing (He et al., 2016). Although its importance is widely recognized, aerosol vertical distribution is very difficult to monitor globally. Lidar is a major technique for obtaining the profiles of the aerosol properties, which has been used in ground-based and satellite remote sensing systems. Especially, spaceborne lidar is an effective way to observe the global distribution of aerosols. The Cloud-Aerosol Lidar with Orthogonal Polarization (CALIOP) on the CALIPSO (The Cloud-Aerosol Lidar and Infrared Pathfinder Satellite Observation) satellite, the only long-term orbiting spaceborne lidar to date, was launched on 28 April 2006. The CALIOP is a three-channel Mie-scattering lidar system, which contains two wavelengths of $532\ nm$ (perpendicular & parallel polarization channel) and $1064\ nm$. It is the first polarization lidar to provide three-channel elastic backscatter signals of global atmospheric measurements. The official aerosol

retrieval algorithm of CALIOP involves three modules, namely the Selective Iterated BoundarY Locator (SIBYL), the Scene Classification Algorithm (SCA), and the Hybrid Extinction Retrieval Algorithms (HERA). The HERA algorithm requires a lidar ratio (extinction-to-backscatter ratio of aerosols), which is provided by the SCA. The SCA uses three CALIOP channels (532 nm parallel, 532 nm perpendicular and 1064 nm channels) to obtain the lidar ratio from the 6 groups of assumed column-averaged lidar ratios based on a clustering of aerosol optical properties measured at surface stations (Winker et al., 2009).

The lidar ratio is dependent on the chemical composition, shape, particle size distribution of aerosols, as well as the lidar wavelength (Burton et al., 2012), which is a critical parameter required for solving the Mie-scattering lidar equation using the Klett (Klett, 1985) or Fernald (Fernald, 1984) methods. Previous studies have developed algorithms to determine the lidar ratio iteratively for two-wavelength Mie scattering lidars. Potter (1987) first introduced the two-wavelength lidar inversion technique to retrieve the aerosol transmission with a constant lidar ratio in two independent wavelengths. Ackermann (Ackermann, 1997, 1998) developed an iterative method to obtain the variable lidar ratio from two-component (i.e., molecule and aerosol) atmospheres by transcendental equation. Rajeev and Parameswaran (1998) proposed a new method using the Mie theory calculated aerosol optical properties with Junge distribution of aerosols to determine the lidar ratio by iteration. Lu et al. (2011) made an attempt to improve the two-wavelength lidar inversion by iterative method, but failed to consider the size distribution of aerosols which may introduce uncertainties in the inversion. Moreover, these studies mostly only gave the aerosol extinction profile without retrieving the vertical distribution of aerosol size information. The algorithms were also mostly applied to theoretical data or ground lidar measurements. The application to space lidars such as CALIOP is challenging and thus limited.

In view of the above discussions, this study aims to provide a modified two-wavelength lidar inversion algorithm to retrieve the vertical distribution of both aerosol extinction and particle effective radius, avoiding the complex calculation confronted in the previous two-wavelength lidar inversion methods. The algorithm is tested on synthetic data, surface Raman lidar and is finally applied to CALIOP measurements,

73 in order to better demonstrate its operational feasibility. The paper proceeds with descriptions of the inversion

74 algorithm in Sect. 2. Sect. 3 presents the application of the algorithm to the Raman lidar and CALIOP with

75 an analysis of retrieval uncertainties provided in Sect. 4. The study concludes in Sect. 5 with a brief discussion

76 in the context of relevant lidar algorithms.

2 Description of the lidar inversion algorithm

78 The modified inversion algorithm retrieves the profiles of aerosol extinction and effective radius at two

79 wavelengths, by solving the lidar equation using the Fernald method (Fernald, 1984) with a look-up table

80 approach in the iteration procedure.

2.1 Solving the lidar equation

82 For each wavelength with a complete overlap between the fields of view of the laser and of the receiver, the

83 lidar equation with calibration and range-correction can be expressed as:

84 $$\beta'(R) = \frac{P(R)R^2}{E_0\xi} = [\beta_m(R) + \beta_p(R)]T_m^2(R)T_p^2(R), \tag{1}$$

85 where

86 $$T^2(R) = e^{-2\tau(R)}, \tag{2}$$

87 $$\tau(R) = \int_{R_0}^{R} \sigma(r)dr, \tag{3}$$

88 In Eq. (1-3), $\beta'(R)$ is the attenuated backscatter coefficients (calibrated and range-corrected signal)

89 from distance R; $P(R)$ is the measured signal after background subtraction and artefact removal from

90 distance R; E_0 is the average laser energy for the single-shot; ξ is the lidar system parameter; $\beta(R)$ and $\sigma(R)$

91 are the volume backscatter and extinction coefficient at range R, respectively; $T^2(R)$ is the two-way

92 transmittance from the lidar to the scattering volume at range R; $\tau(R)$ is the optical depth at range R; and the

93 subscripts M and P denote the portions of air molecules and aerosols, respectively.

94 In order to facilitate calculation, the transmittance of air molecules $T_m^2(R)$ is separated from $\beta'(R)$

95 to obtain the $E(R)$ as

96    $E(R) = \frac{\beta'(R)}{T_m^2(R)},$ (4)

97   As is well known, lidar back scatter signal is also subject to multiple scattering effects. These effects

98   are typically small for low to moderate aerosol loading, and is only significant for optically thick clouds

99   (Winker et al., 2009). Therefore, we neglect multiple scattering effects here and consider that the lidar ratio

100   $(S(R))$ of aerosols is range dependent in single-scatter approximation, which can be written as

101   $S(R) = \frac{\sigma_p(R)}{\beta_p(R)},$ (5)

102   In the following, we use the Fernald method (Ackermann, 1998) to obtain the aerosol extinction

103   coefficient at distance R as

104   $\sigma_p(R) = S(R) \left\{ E(R) e^{-2 \int_{R_0}^{R} S(r) \beta_m(r) dr} \left[C - 2 \int_{R_0}^{R} E(r) S(r) e^{-2 \int_{R_0}^{r} S(r') \beta_m(r') dr'} dr \right]^{-1} - \beta_m(R) \right\},$ ____(6)

105   where

106   $C = \frac{\beta'(R_0)}{\beta_p(R_0) + \beta_m(R_0)},$ (7)

107   The backscatter and extinction coefficient of air molecules can be determined with the Rayleigh

108   scattering theory with the observed atmospheric profile (Bodhaine et al., 1999) as

109   $\sigma_m(R, \lambda) = \frac{C_s(\lambda) P(R)}{T(R)},$ (8)

110   $\beta_m(R, \lambda) = \frac{\sigma_m(R, \lambda)}{\frac{8\pi}{3} k_{b\omega}(\lambda)},$ (9)

111   Where $P(R)$ and $T(R)$ are the atmospheric pressure (hPa) and temperature (K) at distance R, respectively.

112   $C_s(\lambda)$ and $k_{b\omega}(\lambda)$ are the atmospheric molecular constant related to the wavelength λ. Hostetler et al. (2006)

113   suggested the values of $C_s(\lambda)$ and $k_{b\omega}(\lambda)$ at 532 nm and 1064 nm as $C_s(532 \text{ nm}) = 3.742 \times 10^{-6}$ (K/

114   hPa/m); $C_s(1064 \text{ } nm) = 2.265 \times 10^{-7}$ (K/hPa/m); $k_{b\omega}(532 \text{ nm}) = 1.0313$; $k_{b\omega}(1604 \text{ nm}) = 1.0302$.

115   Thus, the aerosol extinction coefficient profiles can be obtained by Eq. (6) with an unknown variable

116   of the lidar ratio. The two-wavelength lidar can give two independent profiles of attenuated backscatter

117 coefficients at different wavelengths, from which the aerosol extinction coefficient profiles can be calculated

118 by assuming the lidar ratios at the two wavelengths.

119   For two wavelengths (λ_1 & λ_2), the Ångström exponent (AE) at distance R is defined as:

120 $$AE(R) = -\frac{ln\left[\frac{\sigma_P(R,\ \lambda_1)}{\sigma_P(R,\ \lambda_2)}\right]}{ln\left[\frac{\lambda_1}{\lambda_2}\right]},$$ (10)

121 Because AE is related to particle size distribution~~effective radius~~, which is a primary factor

122 determining the lidar ratio, an AE-lidar ratio relationship can be established and used to determine the lidar

123 ratio at each layer, which can then be used to retrieve aerosol extinction profiles from two-wavelength lidar

124 measurements.

125 **2.2 Look-up table**

126 By assuming spherical particles size distribution, the aerosol extinction coefficients and backscatter

127 coefficients can be calculated by Eq. (11-12):

128 $$\sigma_p(\lambda) = \int_{r_{min}}^{r_{max}} Q_e(\lambda, r)\, \pi r^2 n(r) dr,$$ (11)

129 $$\beta_p(\lambda) = \int_{r_{min}}^{r_{max}} Q_b(\lambda, r)\, \pi r^2 n(r) dr,$$ (12)

130 Where $n(\mathrm{r})$ represents the volume-size distribution of particles; r_{max} and r_{min} are the maximum and

131 minimum of the particle ~~effective~~ radius, respectively; $Q_e(\lambda, r)$ and $Q_b(\lambda, r)$ denote the extinction and

132 backscatter ~~efficiency~~ efficiencies of the particle (the scatter factor of the particle at 180°) with size r at

133 wavelength λ, respectively. The size parameter is defined as $x \equiv 2\pi \mathrm{r}\ /\ \lambda$, where $1 < x < 50$ for typical

134 aerosols and thus the Mie scattering theory (Mishchenko and Yang, 2018) can be applied.

135   As the limited information provided by two-wavelength lidar, we assume the volume-size distribution

136 of aerosols conform to the lognormal distribution, and the size distribution is expressed as follows (Deshler

137 et al., 2003; Hara et al., 2021):

138 $$n(\mathrm{r}) = \frac{N}{r \ln s_d \sqrt{2\pi}} e^{-\frac{(\ln r - \ln r_0)^2}{2(\ln s_d)^2}},$$ (13)

139 Where N is the total particle concentrations; r_0 and s_d are the median radius and the geometric standard

140 deviation of aerosol size distribution, respectively. ~~When we assumed a constant s_d for the same aerosol type,~~

141 ~~the AE can be calculated with a given r_g value. The particle~~ The particle size distribution is represented by

142 its effective radius ($\bar{r}$) ~~is~~ defined ~~by~~as:

143 $$\bar{r} = \frac{\sum n(\mathrm{r})r^3}{\sum n(\mathrm{r})r^2},\tag{14}$$

144 For convenient calculation, we assume a constant s_d for the each aerosol type, and the relationship between

145 AE and $\bar{r}$ can be established with given r_0 values.

146   We choose the six types of aerosols with their parameters in Table 1, which is consistent with the

147 aerosol classification used in the operational algorithm of CALIOP (Winker et al., 2009). From Table 1, Type

148 3 denotes the scattering aerosols, Type 2 shows both strong scattering and absorption, whereas other types

149 are moderate scattering or absorbing. Combining Eqs. (5, 10-14), the relationship between Ångström

150 exponent (AE) and lidar ratio (S), as well as that between AE and particle effective radius ($\bar{r}$) can be

151 formulated as look-up tables for different refractive indices, as shown in Figure 1. Note that in Figure 1, it is

152 easy to determine $S_{532\,nm}$, $S_{1064\,nm}$ and $\bar{r}$ by the unique AE calculated from the lidar equation for a fixed

153 aerosol type.

154 **2.3 The iterative inversion procedure**

155 After constructing the look-up table, we design the following iterative procedure to simultaneously retrieve

156 aerosol extinction and effective radius profiles. Firstly, we calculate the extinction coefficients ($\sigma_{532\,nm}$ &

157 $\sigma_{1064\,nm}$) of two wavelengths (532 nm & 1064 nm) from an initial guess of the lidar ratios ($S^0_{532\,nm}$ &

158 $S^0_{1064\,nm}$) by solving the lidar equation (Eq. 6), then obtain the Ångström exponent (AE) through Eq. (10).

159 Secondly, the look-up table are used to determine a set of new lidar ratios ($S'_{532\,nm}$ & $S'_{1064\,nm}$), which is

160 used to calculate the new $\sigma_{532\,nm}$ & $\sigma_{1064\,nm}$ and Ångström exponent (AE'). This procedure is repeated until

161 the difference between the updated AE' and previous AE reduces to a very small value (e.g., 10⁻³). The final

162 AE is converted to effective radius from the AE-$\bar{r}$ look-up table, and the final values of $\sigma_{532\,nm}$, $\sigma_{1064\,nm}$,

163 $S_{532\,nm}$, $S_{1064\,nm}$ and $\bar{r}$ are the retrieved results of this layer. The above iterative algorithm is summarized

164 into Figure 2.

165   Although in theory, our algorithm can retrieve aerosol extinction and effective radius at each layer,

166   in reality the measurement noise may cause the inversion of certain layers fail to converge. In these cases,

167   we assume that this layer has the same aerosol type and size distribution as its adjacent layer, and then these

168   two layers are combined into a new layer to continue with the inversion.

169   **2.4 Test of the algorithm with synthetic data**

170   For verifying the feasibility of the inversion algorithm, we first conduct some retrieval tests using synthetic

171   data from Mie scattering and radiative transfer simulations. We assume a hypothesized profile of effective

172   radius, backscatter and extinction coefficients of the aerosols, and use the American atmospheric model in

173   1976 (National Geophysical Data, 1992) for molecular scattering, and calculate the attenuated backscatter

174   profiles according to the lidar equation. We then apply our algorithm to retrieve the aerosol property profiles

175   from these simulated lidar signals and compare them with the initial assumptions.

176   We only present the results for the reflective aerosol model, and results for other aerosol types are

177   similar. The simulated attenuated backscatter profiles for the two wavelengths are shown in Figure 3, and

178   the results of our inversion and their comparison with the assumed profiles are shown in Figure 4. It is clearly

179   seen that the results of the inversion are in good agreement with the assumed profiles. The MAPE (Mean

180   Absolute Percentage Error) between retrieved and assumed profiles of extinction coefficient, average particle

181   effective radius and lidar ratio are all below 0.1%, which proves the validity of the algorithm in theory. Note

182   that typically, selection of aerosol type is critical as incorrect assumption of aerosol refractive index will

183   result in divergence of the algorithm and thus yield no valid retrieval. This also helps us to determine the

184   appropriate aerosol type, i.e., the type that yields the best retrieval results.

185   **3 Application to real lidar measurements**

186   Before applying our algorithm to CALIOP measurements, we first use Raman lidar measurements to test its

187   accuracy as Raman lidars can directly retrieve aerosol extinction profiles without assuming a lidar ratio.

3.1 Application to Raman lidar measurements

A Raman lidar (Model LR231-D300, Raymetrics S.A, Greece) is installed on top of an 8-floor building at the Peking University site (39°59′N, 116°18′E, 53m above sea level). It can provide the extinction and backscatter coefficient at 532 nm by Raman inversion (Ansmann et al., 1990) without the need to assume the lidar ratio. To test our inversion algorithm, we apply it to the elastic backscatter signals at 532 and 1064 nm and compare the retrieved extinction profile at 532 nm with that retrieved with the Raman method. Note that the 1064 nm extinction is estimated using the Angstrom relationship of Eq. (10) and we assume that the 532 ~ 1064 nm AE equals the 355 ~ 532 nm AE. But an approximation of *AE* is used in the inversion at 1064 *nm*, that we approximate the 355 ~ 532 nm AE as the 532 ~ 1064 nm AE to calculate extinction profile at 1064 nm by Eq. (10). We applicate the modified inversion algorithm to the cases of four different aerosol types. To facilitate the determination of the initial value, we use the mothed of remodelling downward attenuated backscatter from ground-based lidar (Tao et al., 2008) to reconstruct the Raman lidar measurements at wavelength of 532 nm and 1064 nm, which are showing Figure 5-8(a).

We examined four cases in December 2017, as shown in Figures 5-8. The cases on 2 and 21 December 2017 both indicate that the extinction coefficient decreases sharply with altitude, and the maximum values occur near the ground (Figure 6b & 7b). The other two cases on December 1 and 23 respectively show the features of an elevated aerosol layer with maximum extinction found above the surface. In all four cases, our retrieval results (red curves) agree well with those retrieved by the Raman method, with MAPE less than 30% in the extinction coefficient profiles. The lidar ratio profiles retrieved by our algorithm also agree well with obtained from Raman method in some ranges, except these spikes at the highest or lowest point, may be caused by the uncertainty of boundary. The aerosol particle effective radius slightly increases with altitude and the peak (corresponding to ~0.1 μm) appear at ~0.7 km and ~1.7 km on 1 and 23 December 2017 (Figure 5d & 8d), respectively. Similar results were found by Zhang et al. (2009) and Cai et al. (2022) with aircraft measurements over Beijing and the Loess Plateau in China respectively, which are mainly associated with long range aerosol transport. The variability of particle effective radius profiles in Figure 6d is a typical

feature for low (and stable) PBL (Planetary Boundary Layer), which results in both particles and water vapor accumulating near PBL top and thus remarkable hygroscopic growth of particle size may occur (Yang et al., 2020). The case for Dec 21 (Figure 7d) shows relatively large particle size below~1.4km but sharply decreases. This is likely related to the domination of local pollutions and insignificant PBL temperature inversion (Li et al., 2022; Liu et al., 2009; Zhang et al., 2009).

3.2 Application to CALIOP measurements

We further apply our algorithm to real CALIOP measurements. To test its performance, we collocate CALIOP profiles with those from surface-based Raman lidar measurement within the European Aerosol Research LIdar NETwork (EARLINET, www.earlinet.org, (Matthias et al., 2004). Aerosol profiles from the Napoli (southern Italy, 40.838 °N , 14.183 °E , 118 m above sea level), Evora (south-central Portugal, 38.5678 °N, −7.9115 °E, 293 m above sea level) and Warsaw (east-central, 52.21 °N, 20.98 °E, 112m above sea level) stations have the best match with CALIOP and high data quality in cloudless sky, are primarily used to validate the retrieval results. The CALIPSO overpass times for the chosen cases and the corresponding horizontal distances between the sub-satellite point and ground-based Raman lidar site are listed in Table 2.

To compare with the lidar returns measured by CALIOP (down-looking) and ground-based Raman lidar (up-looking), we still use the mothed of remodelling downward attenuated backscatter from ground-based lidar (Tao et al., 2008) to reconstruct the downward attenuated backscatter signals for the ground-based Raman lidar. The attenuated backscatter signals of CALIOP was averaged for 163 nearby sub-satellite point profiles (CALIPSO ground track range of about 30 km within 8 s) (Lu et al., 2011; Wang et al., 2007), obtained from CALIOP level 1B products, to improve the signal-to-noise ratio.

The attenuated backscatter profiles at $532\ nm$ from CALIOP agree well with those from the Napoli Raman Lidar (NRL), as shown in Figures 9-14(a). The initial altitude of inversion (the upper boundary of the aerosol layer) is determined by the variation of attenuated backscatter signal and volume linear depolarization

237 ratio at $532 \, nm$. Comparison between our inversion results, CALIOP operational results and Raman results

238 is shown in Figure 9-14(c).

239   The CALIOP operational product only provides retrievals for three cases considered, namely 20

240 August 2006, 20 June 2007 and 22 July 2007. In all three cases, the aerosol extinction profiles of our

241 algorithm (red curve) appear in better consistency with Raman lidar results, and our algorithm ~~cut~~ reduces

242 the mean MAPE between the retrieval of extinction profiles in CALIOP and Raman lidar from 74% (CALIOP

243 operational product) to 37%. Our algorithm successfully corrects the overestimation for the August 20, 2006

244 and July 22, 2007 cases. For the June 20, 2007 case, the operational results show a lower peak at ~1.7 km

245 and a secondary peak at ~4 km, both of which are absent in the Raman profile, and our results agree well

246 with Raman in both the shape and magnitude. In the other three cases, CALIOP does not provide Level 2

247 retrieval results. Our algorithm is able to retrieve and the extinction profiles agree well with Raman lidar

248 observations. Our retrievals do show more fluctuations compared to Raman lidar, possibly due to the noises

249 in the attenuated backscatter profiles of CALIOP. Because Raman lidar does not provide retrieval of aerosol

250 effective radius profiles, we compare the lidar ratio profiles by our algorithm and the Raman algorithm.

251 Overall, our algorithm produces lidar ratios varying in a relatively small range around 50, whereas Raman

252 lidar ratios can vary from ~10 to 200. Also, the Raman lidar ratios tend to change sharply at the highest or

253 lowest point, which may be caused by the inversion errors at the boundary. By removing these spikes, the

254 differences of the lidar ratio between CALIOP and Raman is obviously reduced. In general, the aerosol

255 particle effective radius increases with altitude, similar to Figures 5d and 8d, but the fluctuations of the

256 profiles may also be caused the noise in the CALIOP measurement.

257   When examining the CALIOP backscatter measurements, we found that the backscatter signal at 1064

258 nm is often stronger than that at 532 nm after 2010, which is unphysical and possibly due to issues such as

259 calibration and lidar degradation. As a result, the remodeled backscatter profiles of CALIOP appear noisier

260 and do not exactly match those from Raman lidar for the Evora and Warsaw stations, which only have

261 collocated measurements in 2019 and 2020 (Figure 15-19a). Our retrieved extinction profiles also agree

262 reasonably well with those by Raman lidar (Figure 15-19b), with the lidar ratio profiles and aerosol particle

263 effective radius profiles similar to the cases at Naples. By contrast, the extinction profiles of the official

264 CALIPSO product show large deviations from the Raman profile with unphysical spikes (Figure 16b),

265 incomplete profiles (Figure 17&18b) or no retrievals (Figure 15b).

4 Uncertainty analysis

267 Uncertainties in aerosol extinction and effective radius profiles retrieved by our two-wavelength inversion

268 algorithm are mainly due to measurement noise (e.g., the signal statistical error, the estimations of molecular

269 optical properties, etc.), calibration errors, and assumption errors. In this section, we further examine the

270 errors associated with the assumptions in the algorithm.

271   First, the single-scattering approximation is used in solving lidar equation, as multiple scattering effects

272 in aerosol layers are generally small and are currently neglected for CALIOP (Winker et al., 2009). We limit

273 the application of our algorithm to clear sky weather conditions to reduce this error, but this error is very

274 difficult to quantify.

275   Second, the errors in the aerosol refractive index, size distribution and spherity assumptions in look-up

276 tables can also introduce errors in solving the lidar equation. The lognormal distribution assumption of

277 aerosol volume-size distribution may make the algorithm fail to converge in other actual size distributions.

278 For example, using data generated by Junge distribution (a simpler aerosol size distribution), the algorithm

279 cannot yield valid retrieval results. Similar outcome is noted for non-spherical particles or aerosol types

280 significantly different from the assumed type.

281   Finally, we consider assumption and retrieval uncertainties as a perturbation in the lidar ratio and attempt

282 to quantify its effect on the retrieved profiles. We increase the lidar ratio profiles at 532 nm and 1064 nm

283 from the look-up tables by ±10% before calculating the synthetic attenuated backscatter profiles, which

284 makes the synthetic data do not entirely match the look-up table. The retrieval profiles exhibit mean MAPE

285 less than 14% (in 10% case) and 17% (in -10% case), indicating that the algorithm is comparatively robust

286 to noise.

5 Summary and discussion

288 In this study, we described a modified lidar inversion algorithm to retrieve aerosol extinction and size

289 distribution simultaneously from two wavelengths elastic lidar measurements. Its major advantage over the

290 operational CALIOP algorithm is that the lidar ratio of each layer is determined iteratively by the lidar ratio-

291 AE look-up table. The algorithm was applied to the ground-based Raman lidar measurements at the PKU

292 site, as well as to CALIOP measurements. The comparison results indicate that the retrieved aerosol

293 extinction coefficient profiles by our method using CALIOP attenuated backscatter measurements are in

294 good agreement with Raman lidar measurements. Characteristics of aerosol effective radius profiles are also

295 retrieved, which can be used as a reference for aerosols size information.

296   In comparison with the iterative method by transcendental equation (Ackermann, 1997, 1998), our

297 inversion uses the look-up table to simplify the complex calculation. Cao et al. (2019) develop a lidar-ratio

298 iteration method to invert the particle-size distribution with assumed Junge distribution, but the method was

299 just used in simple simulation without actual tests. Although Lu et al. (2011) invert the aerosol backscatter

300 coefficient profiles from CALIPSO lidar measurements by iterative method, failed to consider the size

301 distribution of aerosols which may introduce uncertainties in the inversion. Compared with other modified

302 CALIOP inversions by combining other measurements, such as ground-based lidar (Wang et al., 2007), our

303 inversion is weaker by the space-time limitations.

304   However, this study still bears certain limitations. The current algorithm is primarily suitable for fine

305 mode spherical particles, such as urban pollution, and considers the change of aerosol size (thus lidar ratio)

306 with altitude, due to long range transport, vertical mixing, hygroscopic growth, etc. Non-spherical particles

307 such as dust will be explored in the next step, possibly by taking advantage of the depolarization ratio

308 (Gialitaki et al., 2020; Kahnert et al., 2020; Luo et al., 2022; Luo et al., 2019) measurement that is not used

here. Another drawback is that although the algorithm does not need to assume a lidar ratio, the complex refractive index still needs to be assumed. As discussed above, the lidar ratio is very sensitive to the imaginary part and an incorrect assumption may induce errors or even makes the algorithm unable to converge. Therefore, this algorithm is mostly suitable when there is no significant change in aerosol type vertically. Finally, the polarization channel of CALIOP may contain additional aerosol type information but is only used when determining the initial refractive index (excluding dust) here. We also plan to refine our look-up table by incorporating polarization in order to improve the accuracy of the retrieval.

Data availability

All raw data can be provided by the corresponding authors upon request.

Author contributions

LC and JL planned the research; LC, JL, JR, CX, and LZ developed the algorithm; LC and JL analyzed the results; LC and JL wrote the manuscript.

Competing interests

The authors declare that they have no conflict of interest.

Acknowledgement

This study is funded by the National Key Research and Development Program of China (grant no. 2023YFF0805401) and National Natural Science Foundation of China (NSFC) Grant No. 42175144.

References

Ackermann, J.: Two-wavelength lidar inversion algorithm for a two-component atmosphere, Appl. Opt., 36, 5134-5143, 10.1364/AO.36.005134, 1997.

Ackermann, J.: Two-wavelength lidar inversion algorithm for a two-component atmosphere with variable extinction-to-backscatter ratios, Appl. Opt., 37, 3164-3171, 10.1364/AO.37.003164, 1998.

Ansmann, A., Riebesell, M., and Weitkamp, C.: Measurement of atmospheric aerosol extinction profiles with a Raman lidar, Opt. Lett., 15, 746-748, 10.1364/OL.15.000746, 1990.

Bodhaine, B. A., Wood, N. B., Dutton, E. G., and Slusser, J. R.: On Rayleigh Optical Depth Calculations, Journal of Atmospheric and Oceanic Technology, 16, 1854-1861, 10.1175/1520-0426(1999)016<1854:orodc>2.0.co;2, 1999.

Burton, S. P., Ferrare, R. A., Hostetler, C. A., Hair, J. W., Rogers, R. R., Obland, M. D., Butler, C. F., Cook, A. L., Harper, D. B., and Froyd, K. D.: Aerosol classification using airborne High Spectral Resolution Lidar measurements – methodology and examples, Atmos. Meas. Tech., 5, 73-98, 10.5194/amt-5-73-2012, 2012.

Cai, Z., Li, Z., Li, P., Li, J., Sun, H., Yang, Y., Gao, X., Ren, G., Ren, R., and Wei, J.: Vertical distributions of aerosol microphysical and optical properties based on aircraft measurements made over the Loess Plateau in China, Atmospheric Environment, 270, 118888, https://doi.org/10.1016/j.atmosenv.2021.118888, 2022.

Cao, N., Yang, S., Cao, S., Yang, S., and Shen, J.: Accuracy calculation for lidar ratio and aerosol size distribution by dual-wavelength lidar, Applied Physics A, 125, 590, 10.1007/s00339-019-2819-y, 2019.

Deshler, T., Hervig, M. E., Hofmann, D. J., Rosen, J. M., and Liley, J. B.: Thirty years of in situ stratospheric aerosol size distribution measurements from Laramie, Wyoming (41°N), using balloon-borne instruments, Journal of Geophysical Research: Atmospheres, 108, 10.1029/2002jd002514, 2003.

Eswaran, K., Satheesh, S. K., and Srinivasan, J.: Sensitivity of aerosol radiative forcing to various aerosol parameters over the Bay of Bengal, Journal of Earth System Science, 128, 170, 10.1007/s12040-019-1200-z, 2019.

Fernald, F. G.: Analysis of atmospheric lidar observations: some comments, Appl. Opt., 23, 652-653, 10.1364/AO.23.000652, 1984.

Gialitaki, A., Tsekeri, A., Amiridis, V., Ceolato, R., Paulien, L., Kampouri, A., Gkikas, A., Solomos, S., Marinou, E., Haarig, M., Baars, H., Ansmann, A., Lapyonok, T., Lopatin, A., Dubovik, O., Groß, S., Wirth, M., Tsichla, M., Tsikoudi, I., and Balis, D.: Is the near-spherical shape the "new black" for smoke?, Atmos. Chem. Phys., 20, 14005-14021, 10.5194/acp-20-14005-2020, 2020.

Goto, D., Nakajima, T., Takemura, T., and Sudo, K.: A study of uncertainties in the sulfate distribution and its radiative forcing associated with sulfur chemistry in a global aerosol model, Atmos. Chem. Phys., 11, 10889-10910, 10.5194/acp-11-10889-2011, 2011.

Hara, K., Nishita-Hara, C., Osada, K., Yabuki, M., and Yamanouchi, T.: Characterization of aerosol number size distributions and their effect on cloud properties at Syowa Station, Antarctica, Atmos. Chem. Phys., 21, 12155-12172, 10.5194/acp-21-12155-2021, 2021.

He, Q., Li, C., Geng, F., Zhou, G., Gao, W., Yu, W., Li, Z., and Du, M.: A parameterization scheme of aerosol vertical distribution for surface-level visibility retrieval from satellite remote sensing, Remote Sensing of Environment, 181, 1-13, https://doi.org/10.1016/j.rse.2016.03.016, 2016.

Hostetler, C., Liu, Z., Reagan, J., Vaughan, M., Winker, D., Osborn, M., Hunt, W., Powell, K., and Trepte, C.: CALIOP algorithm theoretical basis document calibration and Level 1 data products, Hampton, VA: NASA Langley Research Center, 2006.

IPCC: Climate Change 2021 – The Physical Science Basis: Working Group I Contribution to the Sixth Assessment Report of the Intergovernmental Panel on Climate Change, Cambridge University Press, Cambridge, DOI: 10.1017/9781009157896, 2023.

374 Josset, D., Rogers, R., Pelon, J., Hu, Y., Liu, Z., Omar, A., and Zhai, P.-W.: CALIPSO lidar ratio retrieval

375   over the ocean, Opt. Express, 19, 18696-18706, 10.1364/OE.19.018696, 2011.

376 Kahnert, M., Kanngießer, F., Järvinen, E., and Schnaiter, M.: Aerosol-optics model for the backscatter

377   depolarisation ratio of mineral dust particles, Journal of Quantitative Spectroscopy and Radiative

378   Transfer, 254, 107177, https://doi.org/10.1016/j.jqsrt.2020.107177, 2020.

379 Klett, J. D.: Lidar inversion with variable backscatter/extinction ratios, Appl. Opt., 24, 1638-1643,

380   10.1364/AO.24.001638, 1985.

381 Kudo, R., Nishizawa, T., and Aoyagi, T.: Vertical profiles of aerosol optical properties and the solar heating

382   rate estimated by combining sky radiometer and lidar measurements, Atmos. Meas. Tech., 9, 3223-

383   3243, 10.5194/amt-9-3223-2016, 2016.

384 Li, Y., Guo, X., Jin, L., Li, P., Sun, H., Zhao, D., and Ma, X.: Aircraft Measurements of Summer Vertical

385   Distributions of Aerosols and Transitions to Cloud Condensation Nuclei and Cloud Droplets in

386   Central Northern China, Chinese Journal of Atmospheric Sciences, 46, 845, 10.3878/j.issn.1006-

387   9895.2104.20255, 2022.

388 Liu, P., Zhao, C., Zhang, Q., Deng, Z., Huang, M., Ma, X., and Tie, X.: Aircraft study of aerosol vertical

389   distributions over Beijing and their optical properties, Tellus B, 61, 756-767,

390   https://doi.org/10.1111/j.1600-0889.2009.00440.x, 2009.

391 Lu, X., Jiang, Y., Zhang, X., Wang, X., and Spinelli, N.: Two-wavelength lidar inversion algorithm for

392   determination of aerosol extinction-to-backscatter ratio and its application to CALIPSO lidar

393   measurements, Journal of Quantitative Spectroscopy and Radiative Transfer, 112, 320-328,

394   https://doi.org/10.1016/j.jqsrt.2010.07.013, 2011.

395 Luo, J., Zhang, Q., Luo, J., Liu, J., Huo, Y., and Zhang, Y.: Optical Modeling of Black Carbon With Different

396   Coating Materials: The Effect of Coating Configurations, Journal of Geophysical Research:

397   Atmospheres, 124, 13230-13253, https://doi.org/10.1029/2019JD031701, 2019.

398 Luo, J., Li, Z., Fan, C., Xu, H., Zhang, Y., Hou, W., Qie, L., Gu, H., Zhu, M., Li, Y., and Li, K.: The
399   polarimetric characteristics of dust with irregular shapes: evaluation of the spheroid model for single
400   particles, Atmos. Meas. Tech., 15, 2767-2789, 10.5194/amt-15-2767-2022, 2022.

401 Matthias, V., Freudenthaler, V., Amodeo, A., Balin, I., Balis, D., Bosenberg, J., Chaikovsky, A., Chourdakis,
402   G., Comeron, A., Delaval, A., De Tomasi, F., Eixmann, R., Hagard, A., Komguem, L., Kreipl, S.,
403   Matthey, R., Rizi, V., Rodrigues, J., Wandinger, U., and Wang, X.: Aerosol lidar intercomparison in
404   the framework of the EARLINET project. 1. Instruments (vol 43, pg 976, 2004), Appl. Opt., 43, 2004.

405 Mishchenko, M. I. and Yang, P.: Far-field Lorenz–Mie scattering in an absorbing host medium: Theoretical
406   formalism and FORTRAN program, Journal of Quantitative Spectroscopy and Radiative Transfer,
407   205, 241-252, https://doi.org/10.1016/j.jqsrt.2017.10.014, 2018.

408 National Geophysical Data, C.: U.S. standard atmosphere (1976), Planetary and Space Science, 40, 553-554,
409   https://doi.org/10.1016/0032-0633(92)90203-Z, 1992.

410 Potter, J. F.: Two-frequency lidar inversion technique, Appl. Opt., 26, 1250-1256, 10.1364/AO.26.001250,
411   1987.

412 Rajeev, K. and Parameswaran, K.: Iterative method for the inversion of multiwavelength lidar signals to
413   determine aerosol size distribution, Appl. Opt., 37, 4690-4700, 10.1364/AO.37.004690, 1998.

414 Tao, Z., McCormick, M. P., and Wu, D.: A comparison method for spaceborne and ground-based lidar and
415   its application to the CALIPSO lidar, Applied Physics B, 91, 639, 10.1007/s00340-008-3043-1, 2008.

416 Wang, X., Frontoso, M. G., Pisani, G., and Spinelli, N.: Retrieval of atmospheric particles optical properties
417   by combining ground-based and spaceborne lidar elastic scattering profiles, Opt. Express, 15, 6734-
418   6743, 10.1364/OE.15.006734, 2007.

419 Winker, D. M., Vaughan, M. A., Omar, A., Hu, Y., Powell, K. A., Liu, Z., Hunt, W. H., and Young, S. A.:
420   Overview of the CALIPSO Mission and CALIOP Data Processing Algorithms, Journal of
421   Atmospheric and Oceanic Technology, 26, 2310-2323, 10.1175/2009jtecha1281.1, 2009.

422 Yang, J., Li, J., Li, P., Sun, G., Cai, Z., Yang, X., Cui, C., Dong, X., Xi, B., Wan, R., Wang, B., and Zhou,

423   Z.: Spatial Distribution and Impacts of Aerosols on Clouds Under Meiyu Frontal Weather

424   Background Over Central China Based on Aircraft Observations, Journal of Geophysical Research:

425   Atmospheres, 125, e2019JD031915, https://doi.org/10.1029/2019JD031915, 2020.

426 Zhang, L., Li, J., Jiang, Z., Dong, Y., Ying, T., and Zhang, Z.: Clear-Sky Direct Aerosol Radiative Forcing

427   Uncertainty Associated with Aerosol Optical Properties Based on CMIP6 Models, Journal of Climate,

428   35, 3007-3019, https://doi.org/10.1175/JCLI-D-21-0479.1, 2022.

429 Zhang, Q., Ma, X., Tie, X., Huang, M., and Zhao, C.: Vertical distributions of aerosols under different

430   weather conditions: Analysis of in-situ aircraft measurements in Beijing, China, Atmospheric

431   Environment, 43, 5526-5535, https://doi.org/10.1016/j.atmosenv.2009.05.037, 2009.

432

433

434 **Table 1.** The aerosols parameters of the look-up table. m_r denotes the real part of the refractive index, m_i

435 denotes the imaginary part of the refractive index, and s_d is the standard deviation of the lognormal size

436 distribution.

	Type 1	Type 2	Type 3	Type 4	Type 5	Type 6
m_r (532 nm)	1.414	1.517	1.380	1.404	1.400	1.452
m_i (532 nm)	0.0036	0.0234	0.0001	0.0063	0.0050	0.0109
m_r (1064 nm)	1.495	1.541	1.380	1.439	1.400	1.512
m_i (1064 nm)	0.0043	0.0298	0.0001	0.0073	0.0050	0.0137
s_d	1.4813	1.5624	1.6100	1.5257	1.6000	1.5112

437

438 **Table 2.** Information of collocated EARLINET and CALIPSO cases.

439

Station	Time (UTC)	Horizontal distance (km)
Napoli	**2006-08-20 01:17:25**	0.0708
	2007-06-20 01:17:57	0.0808
	2008-07-08 01:18:43	0.0690
	2008-08-02 01:13:02	1.3246
	2008-08-09 01:19:14	0.0807
	2009-09-29 01:21:03	0.0778
Evora	**2019-04-05 02:47:48**	0.0863
	2020-01-13 02:54:00	0.0164
	2020-03-18 02:55:43	0.0009
Warsaw	**2015-08-15 01:19:14**	< 0.0001
	2020-03-31 01:13:38	0.0177

440
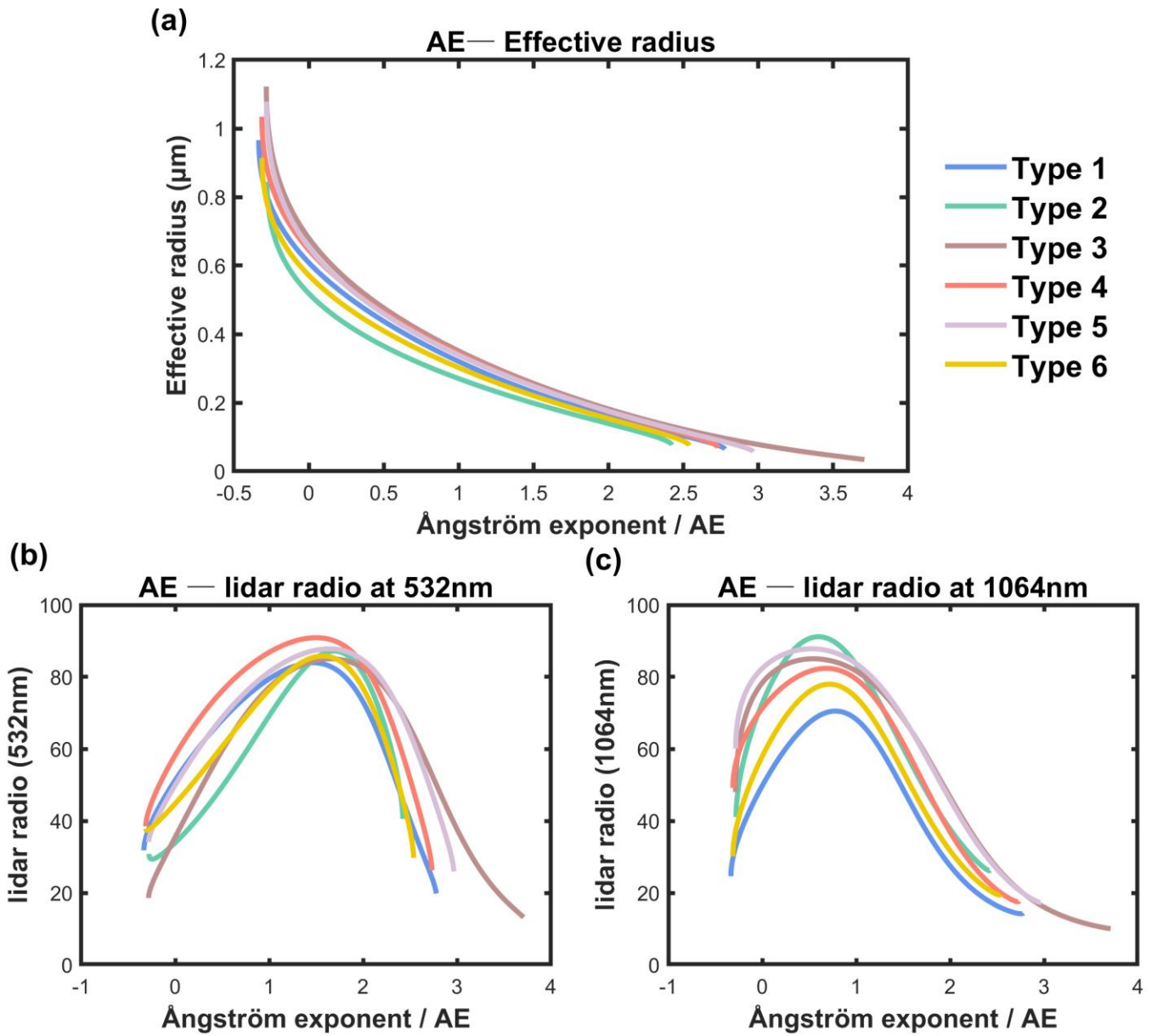
Figure 1. The Look-up tables for (a) AE-effective radius, (b) AE-lidar ratio at 532 nm532 nm and (c) AE-

lidar ratio at 1064 nm. The AE is calculated using 532 nm532 nm and 1064 nm aerosol extinction coefficients.

443
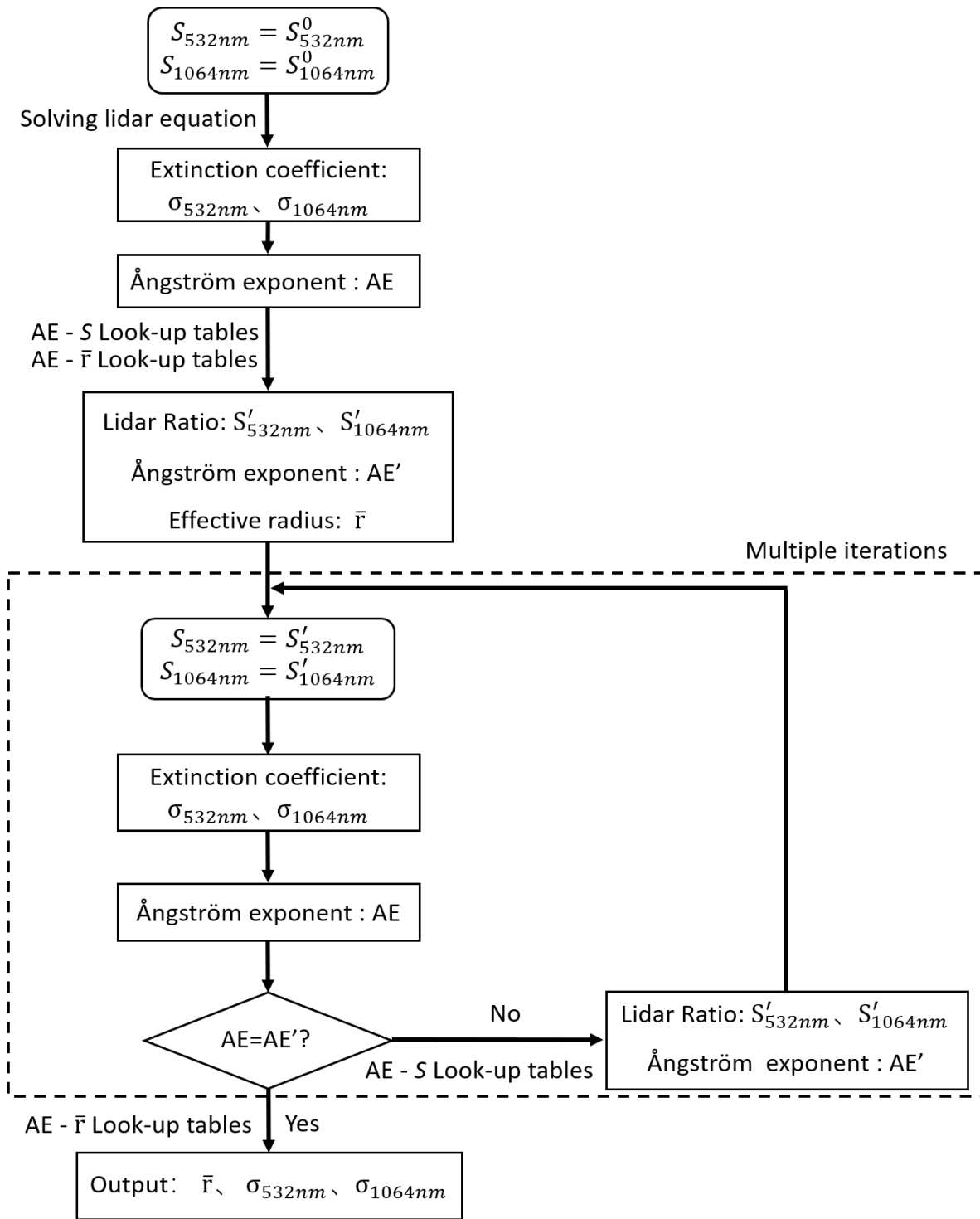
Figure 2. Schematic of the inversion algorithm (λ_1 and λ_2 represent the two different wavelengths, respectively; S is the lidar ratio; σ is the aerosol extinction; AE is the Ångström index; $\bar{r}$ is the average particle effective radius; S^0 is the initial value of lidar ratio; S' and AE′ are the look up values of lidar ratio and Ångström index, respectively.)
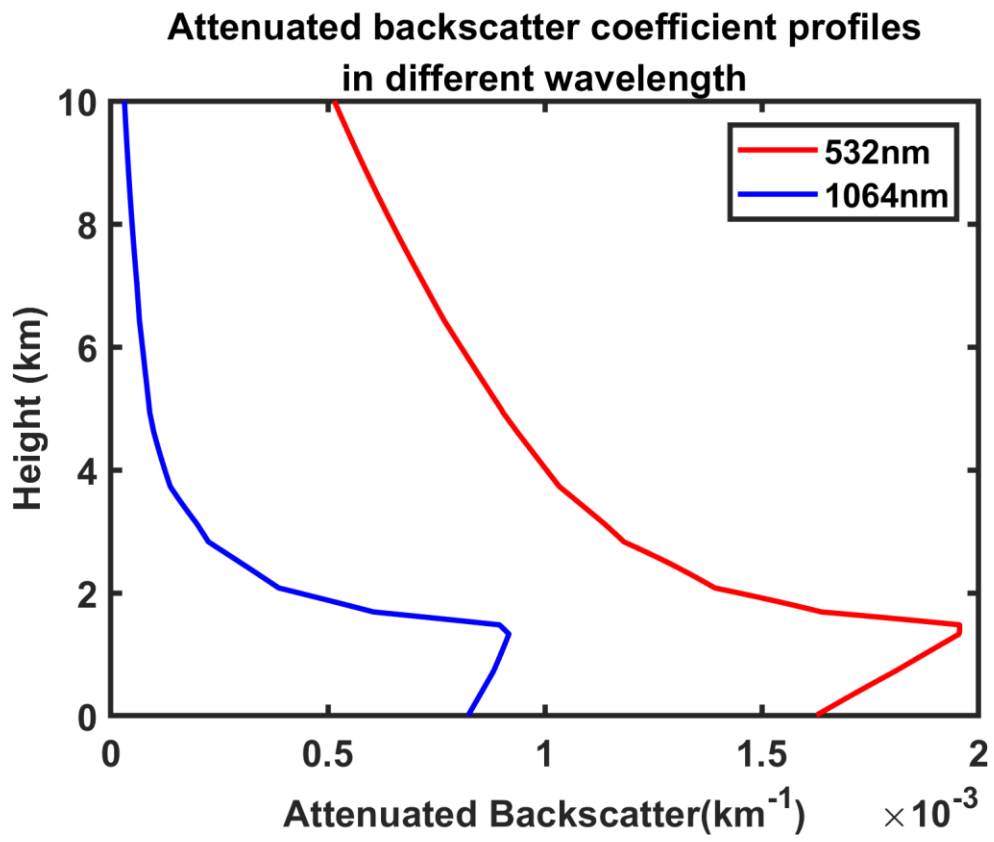
448

449 **Figure 3.** The attenuated backscatter coefficient profiles at different wavelengths using synthetic data.

450
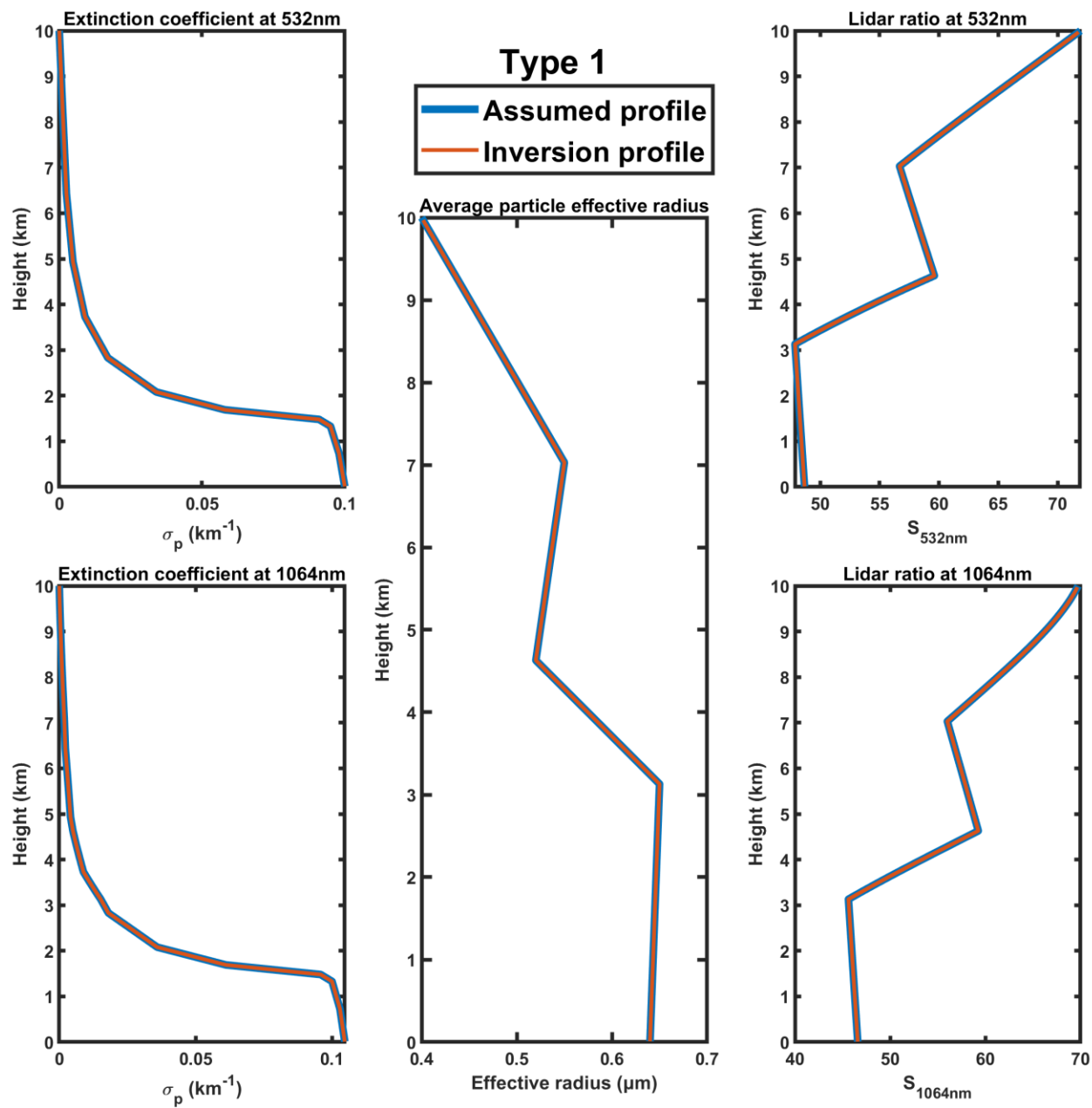
Figure 4. The result of the inversion algorithm using the synthetic data shown in Figure 3.

452
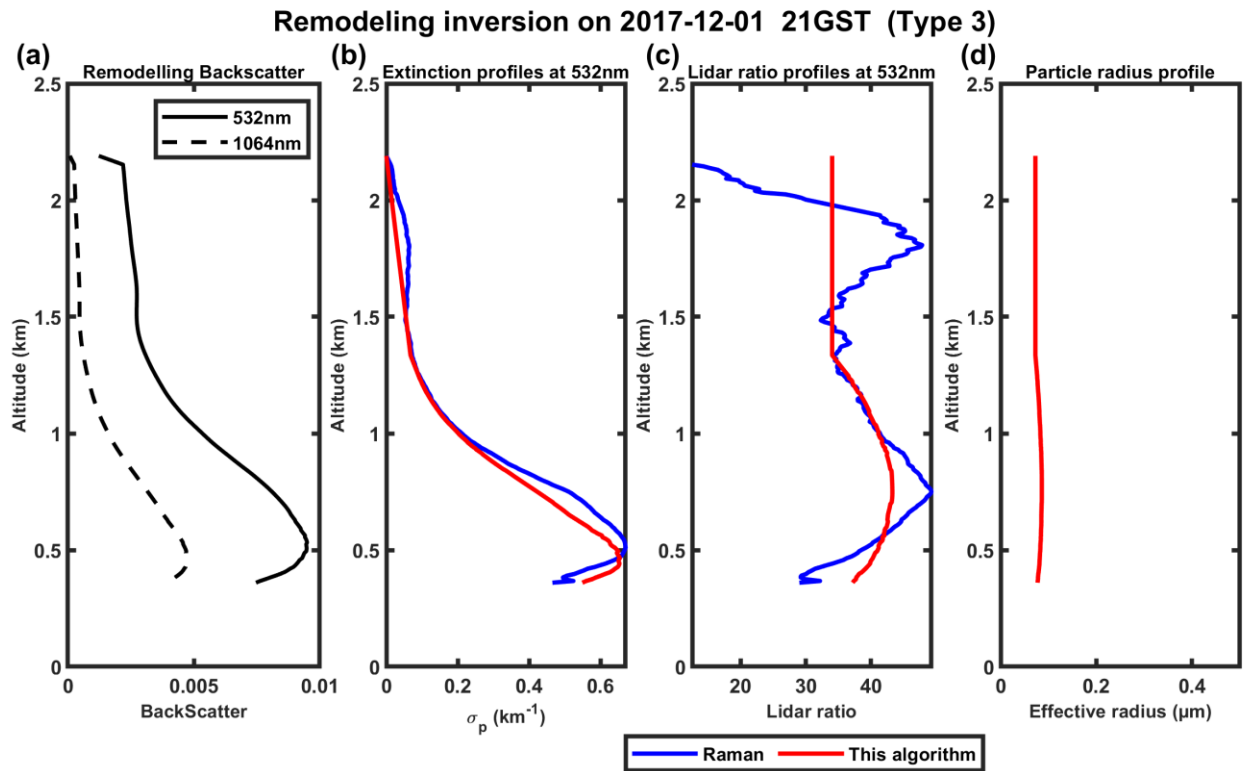
Figure 5. (a) Remodeled downward attenuated backscatter profiles measured by Raman lidar in PKU on 1

December 2017; (b) show the extinction profiles inversed by the modified inversion algorithm (red) and

Raman (blue); (c) shows the particle effective radius profiles.

456
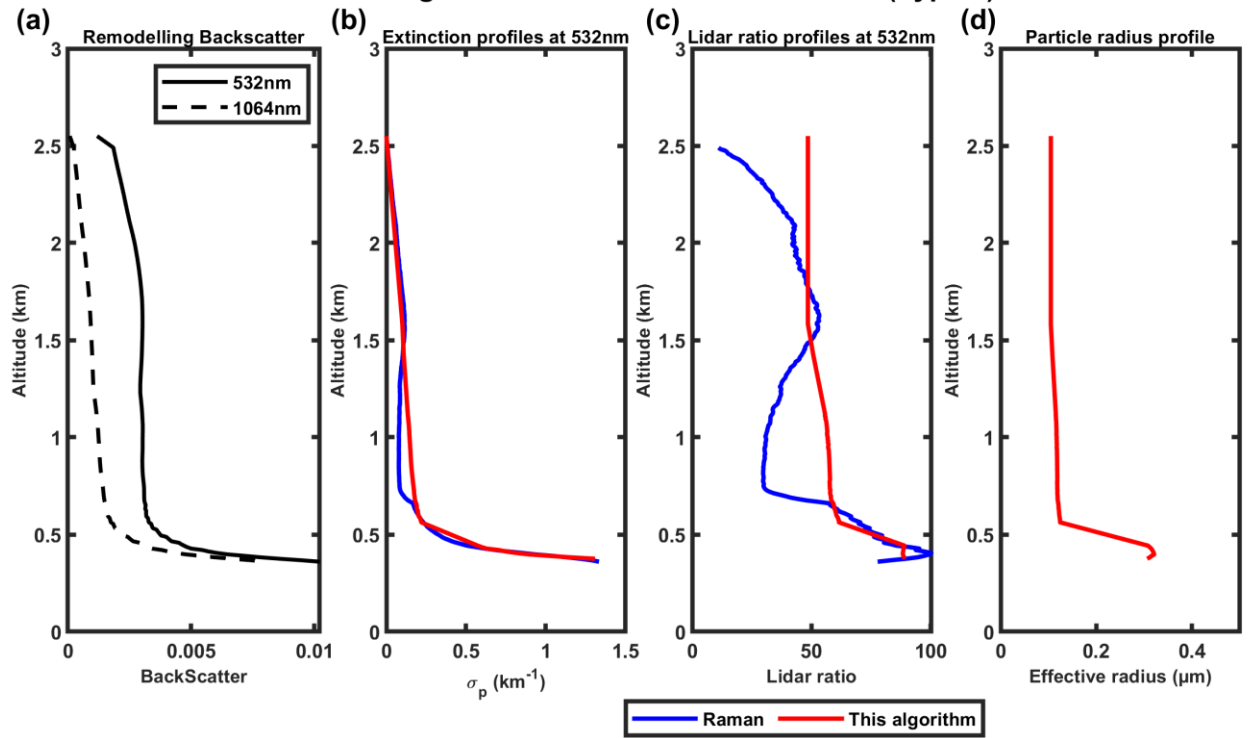
Figure 6. Same as Figure 5 but on 2 December 2017.
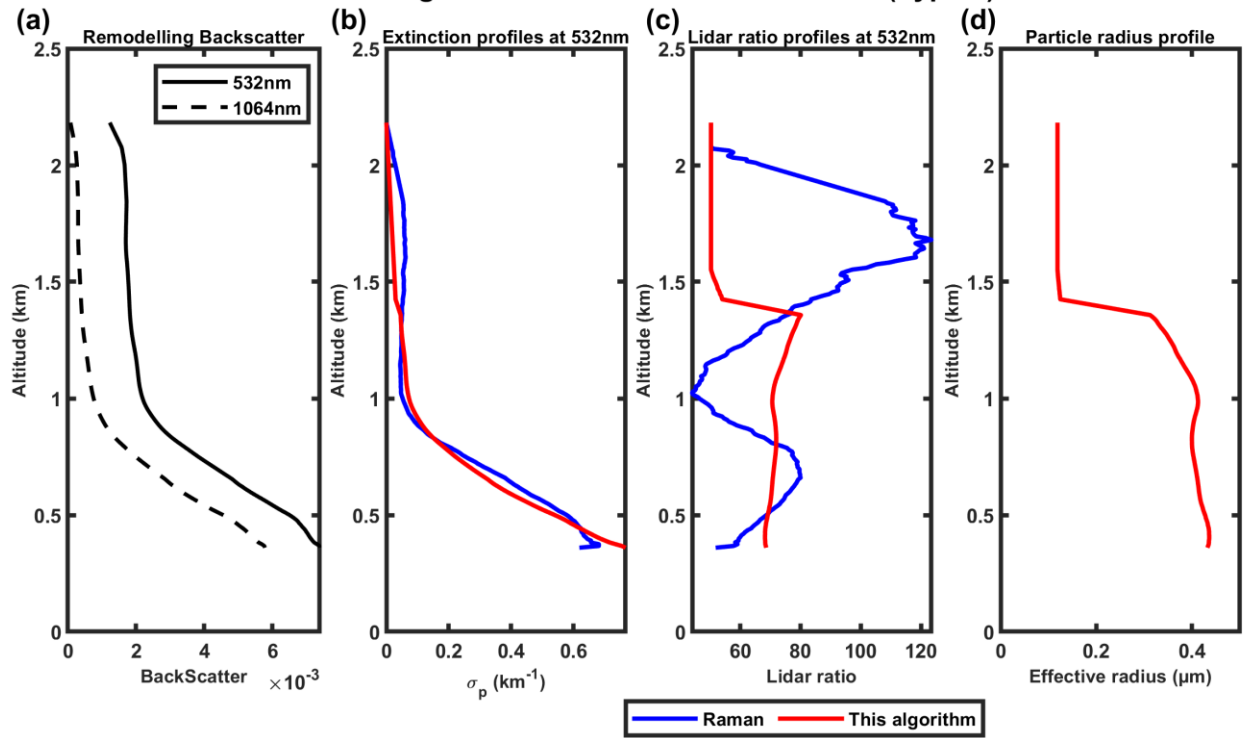
Figure 7. Same as Figure 5 but on 21 December 2017.

463
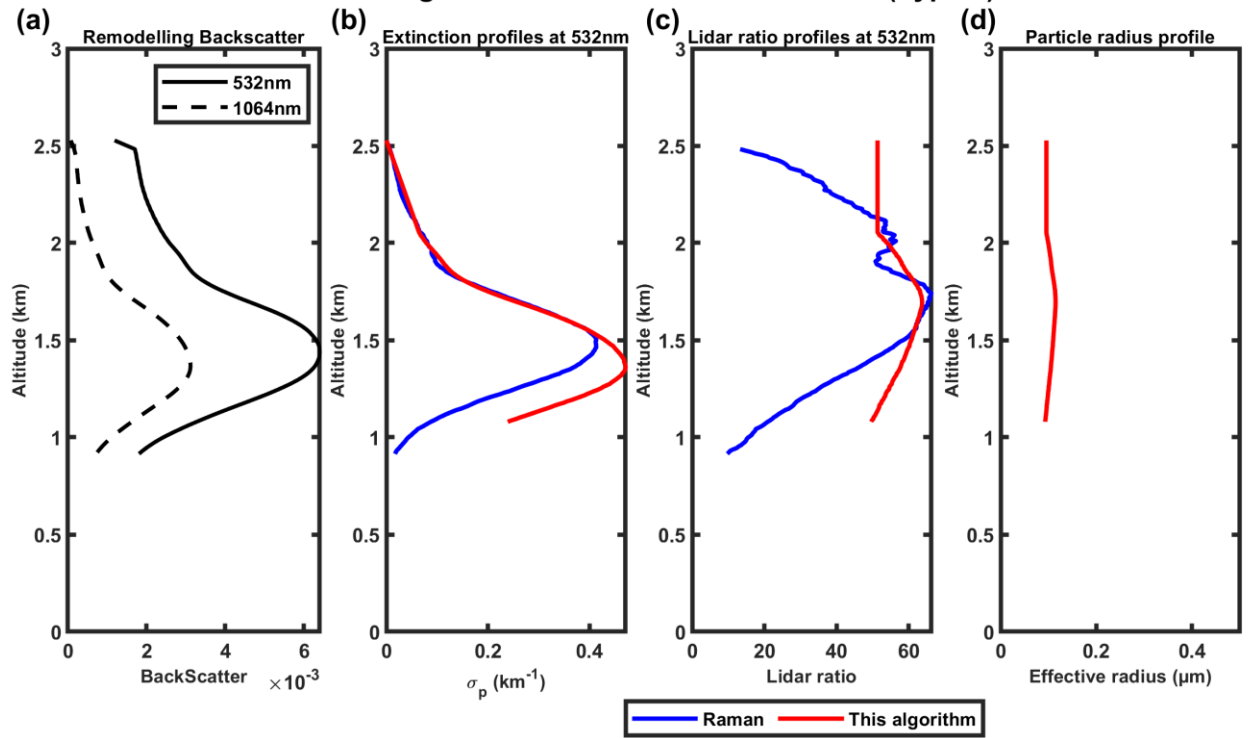
Figure 8. Same as Figure 5 but on 23 December 2017.

465

466
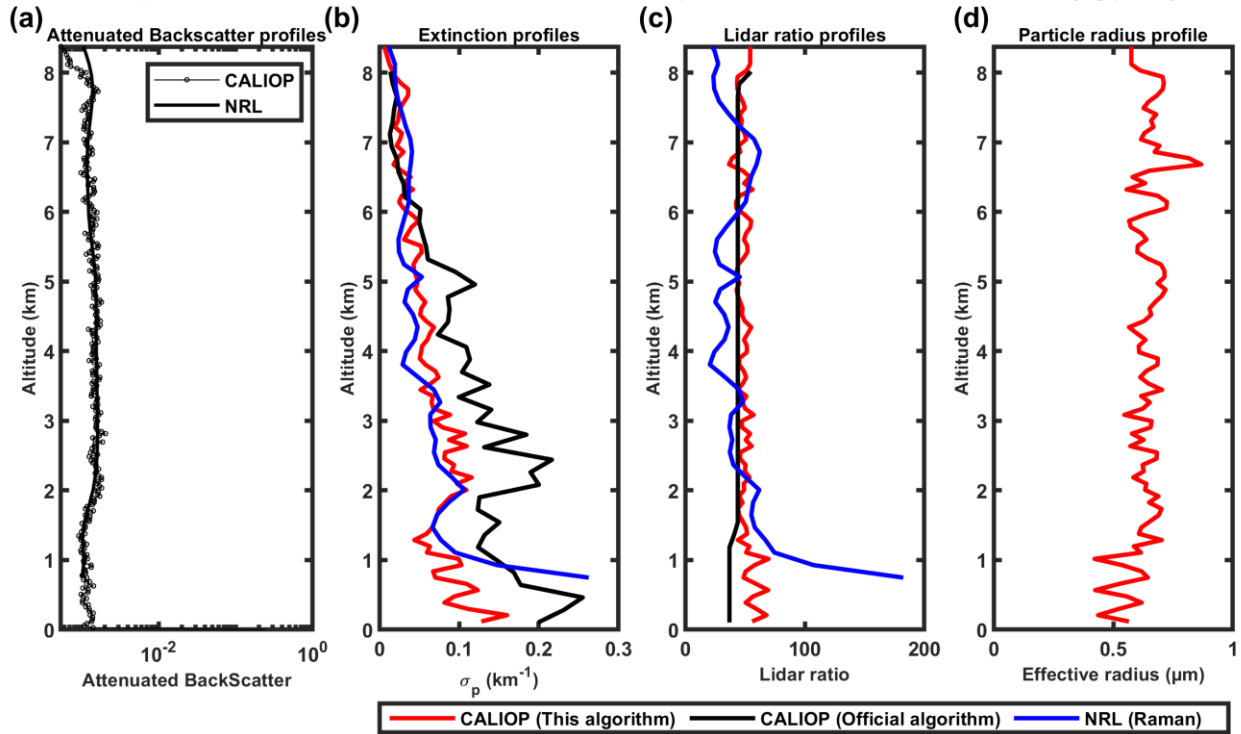
Figure 9. 532 nm and 1064 nm attenuated backscatter profiles measured by CALIOP (black solid line with

circle marker) and NRL (remodeling, black solid line) on 20 August 2006 in logarithmic scale in horizontal

direction (a); (b, c, d) show the extinction profiles, lidar ratio profiles and particle radius profiles, respectively,

provided by our inversion algorithm (red), CALIOP operational level 2 product (black) and EARLINET level

2 product (blue).

Comparsion of CALIOP and EARLINET in Naples at 532nm on 2007-06-20 (Type 5)

(a) Attenuated Backscatter profiles **(b)** Extinction profiles **(c)** Lidar ratio profiles **(d)** Particle radius profile

Figure with four panels showing profiles of Altitude (km) versus Attenuated BackScatter, σ_p (km^{-1}), Lidar ratio, and Effective radius (µm). Legends: CALIOP, NRL; CALIOP (This algorithm), CALIOP (Official algorithm), NRL (Raman).
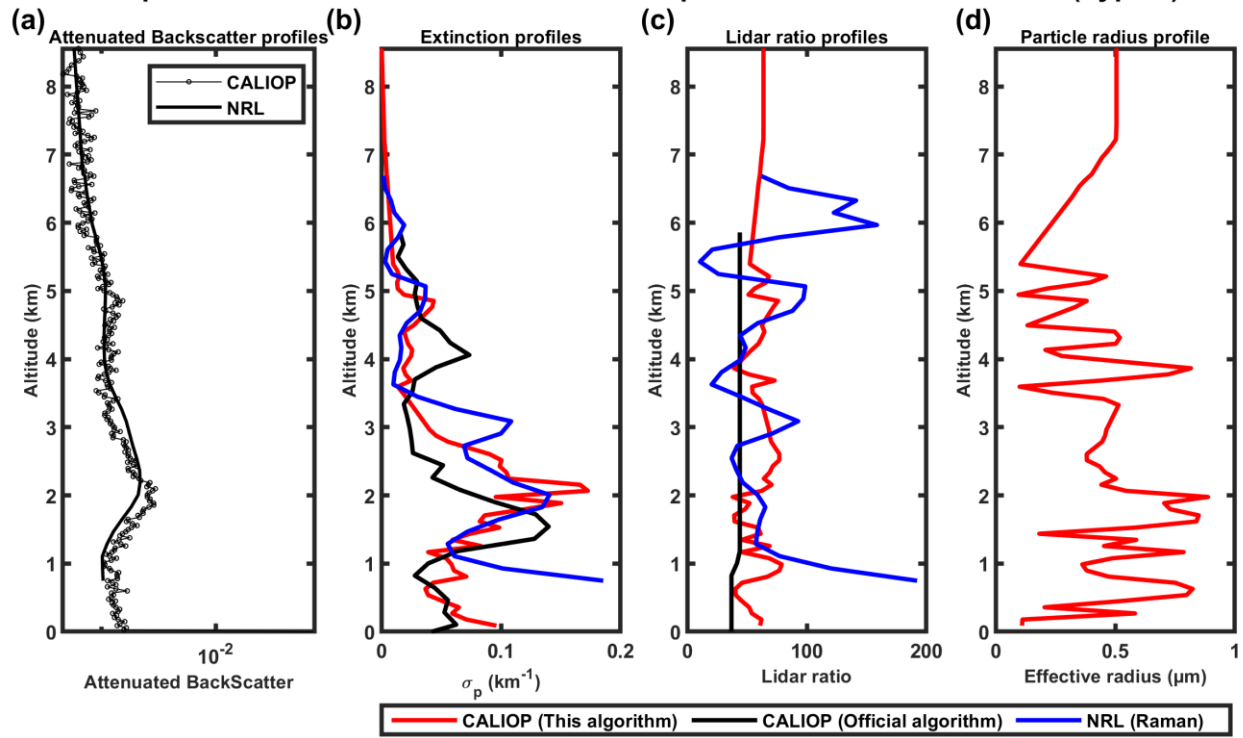
Figure 10. Same as Figure 9 but on 20 June 2007.

Comparsion of CALIOP and EARLINET in Naples at 532nm on 2007-07-22 (Type 6)

475
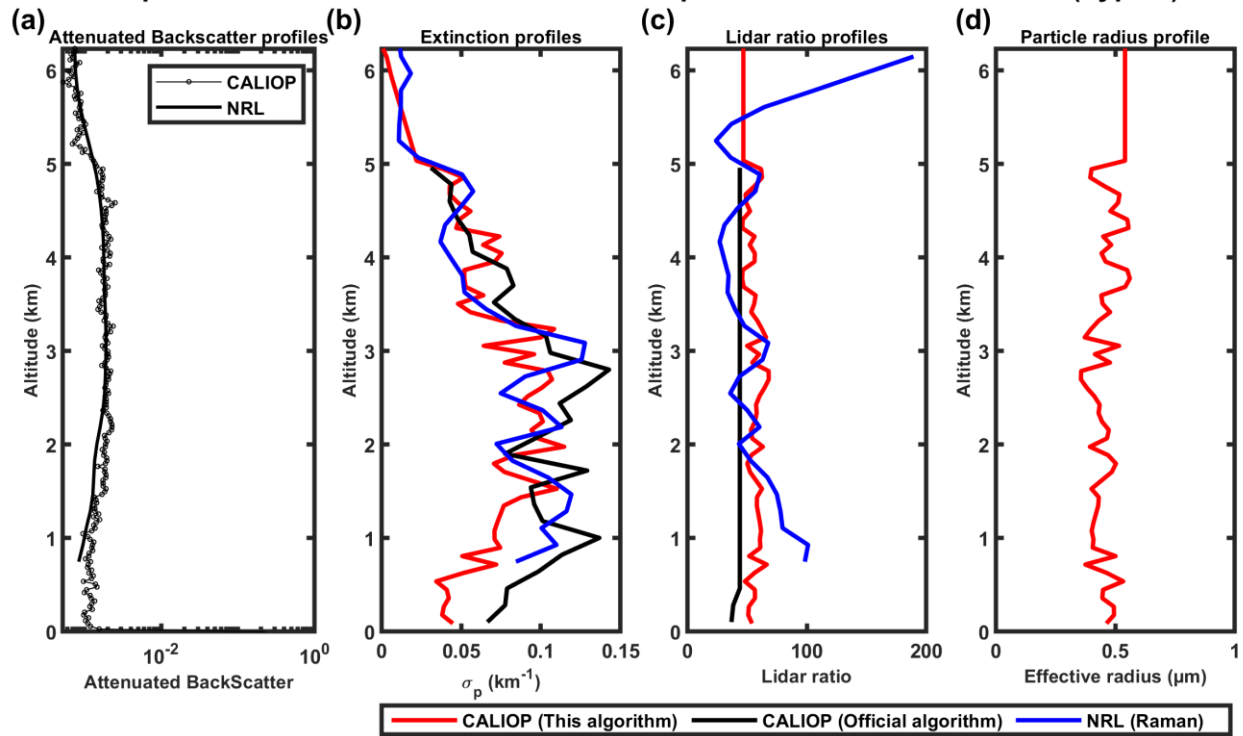
Figure 11. Same as Figure 9 but on 22 July 2007.

477

478

479
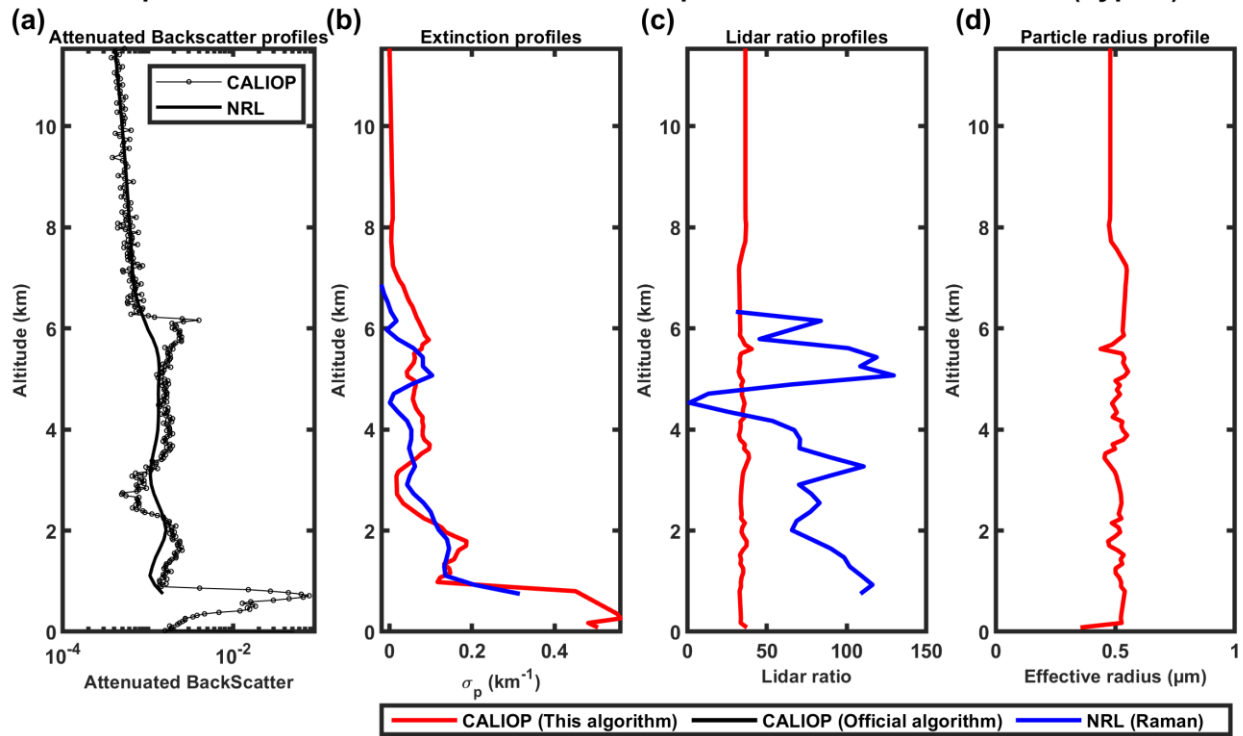
480   **Figure 12.** Same as Figure 9 but on 8 July 2008.

481

Comparsion of CALIOP and EARLINET in Naples at 532nm on 2008-08-09 (Type 3)

482
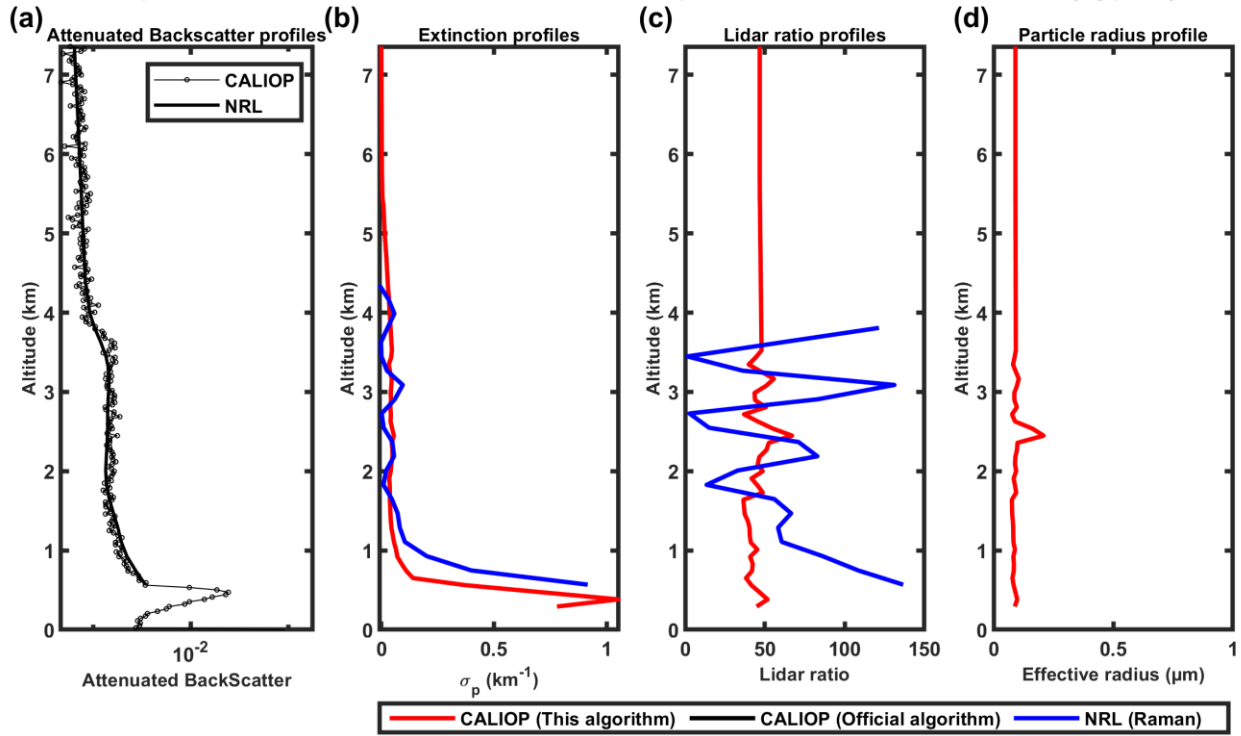
Figure 13. Same as Figure 9 but on 9 August 2008.

484

Comparsion of CALIOP and EARLINET in Naples at 532nm on 2009-09-29 (Type 4)

485
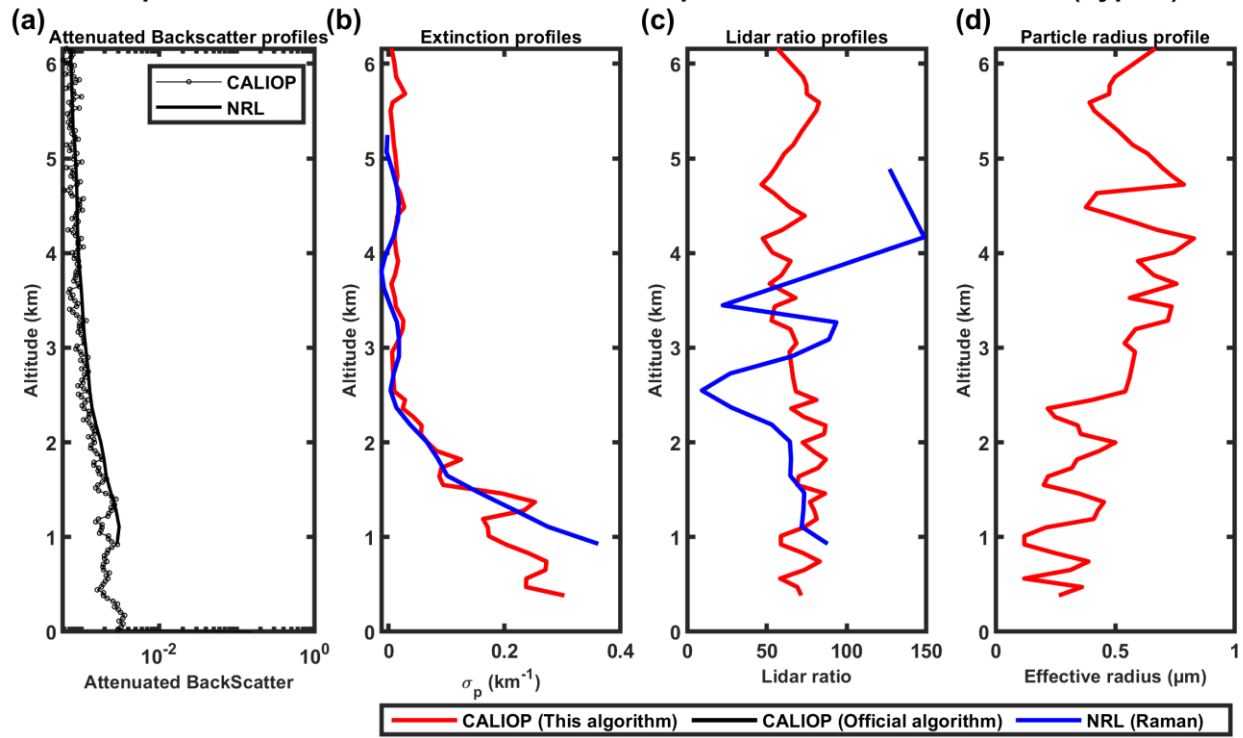
486   **Figure 14.** Same as Figure 9 but on 29 September 2009.

487

Figure 15. 532 nm and 106 nm attenuated backscatter profiles measured by CALIOP (black solid line with circle marker) and ERL at the Evora station (remodeling, black solid line) on 20 August 2006 in logarithmic scale in horizontal direction (a); (b, c, d) show the extinction profiles, lidar ratio profiles and particle radius profiles, respectively, provided by the modified inversion algorithm (red), CALIOP level 2 (black) and EARLINET level 2 (blue).

Figure 16. Same as Figure 15 but on 13 January 2020.

Comparsion of CALIOP and EARLINET in Evora at 532nm on 2020-03-18 (Type 6)

497
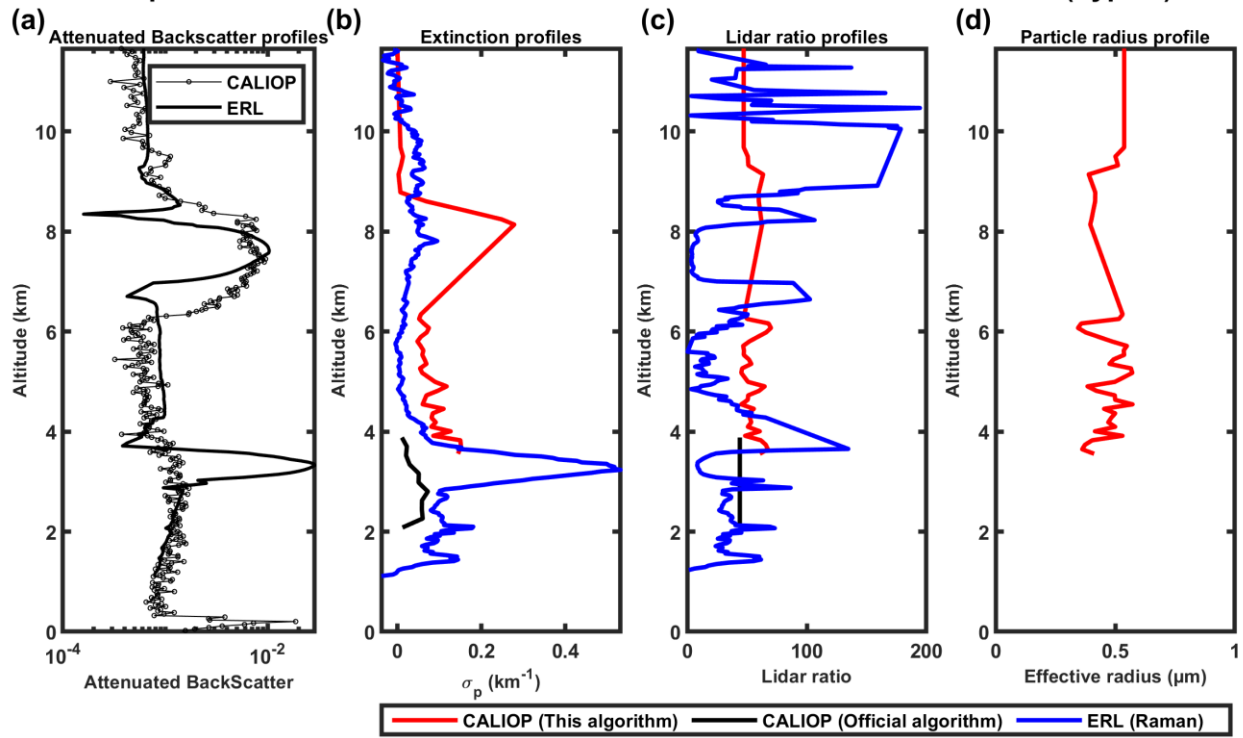
498   **Figure 17.** Same as Figure 15 but on 18 March 2020.

499
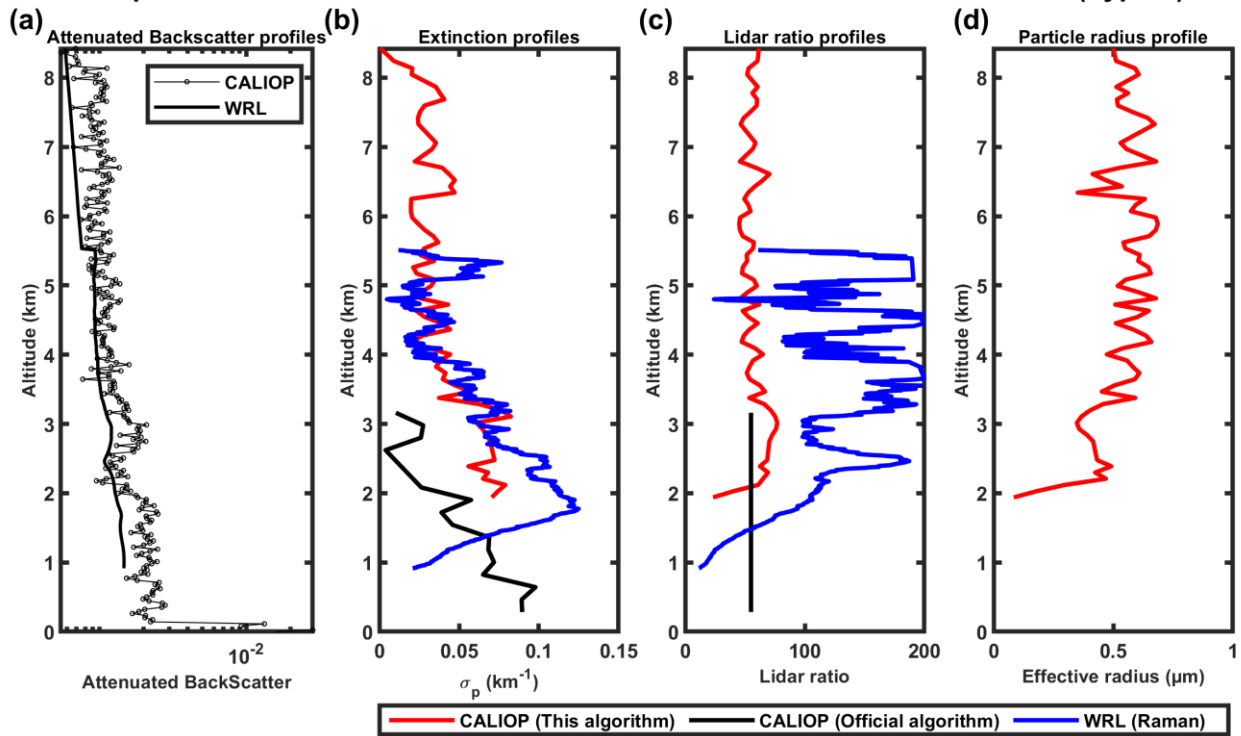
Figure 18. 532 nm and 106 nm attenuated backscatter profiles measured by CALIOP (black solid line with circle marker) and WRL at the Warsaw station (remodeling, black solid line) on 20 August 2006 in logarithmic scale in horizontal direction (a); (b, c, d) show the extinction profiles, lidar ratio profiles and particle radius profiles, respectively, provided by the modified inversion algorithm (red), CALIOP level 2 (black) and EARLINET level 2 (blue).

506
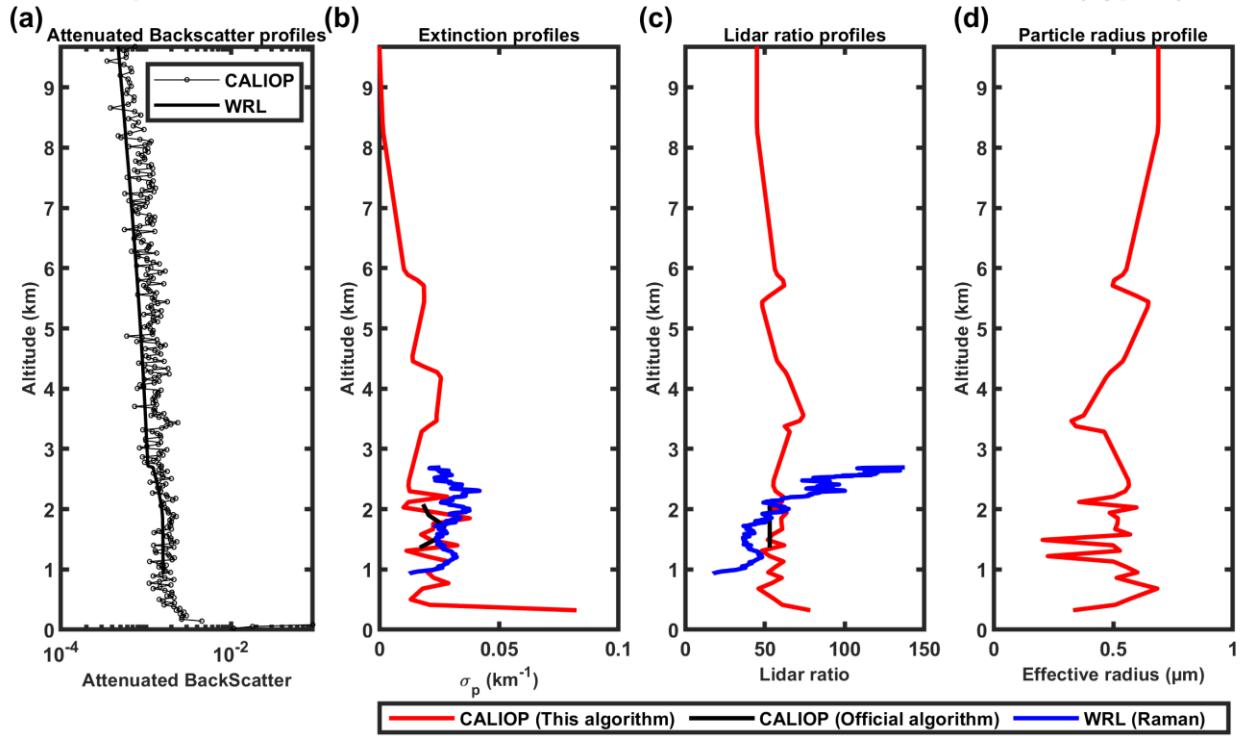
Figure 19. Same as Figure 18 but on 31 March 2020.

508